Available online at www.sciencedirect.com
ScienceDirect
Chemical Physics 329 (2006) 230–238
Chemical Physics
www.elsevier.com/locate/chemphys

# Free tetra- and hexa-coordinated platinum-cyanide dianions, $Pt(CN)_4^{2-}$ and $Pt(CN)_6^{2-}$: A combined photodetachment photoelectron spectroscopic and theoretical study

Xue-Bin Wang [a,b], Yi-Lei Wang [c], Hin-Koon Woo [a,b], Jun Li [c,*], Guo-Shi Wu [c], Lai-Sheng Wang [a,b,*]

[a] Department of Physics, Washington State University, 2710 University Drive, Richland, WA 99354, USA
[b] Chemical Sciences Division, Pacific Northwest National Laboratory, MS K8-88, P.O. Box 999, Richland, WA 99352, USA
[c] Department of Chemistry and Key Laboratory of Organic Optoelectronics and Molecular Engineering of Ministry of Education, Tsinghua University, Beijing 100084, China

Received 23 May 2006; accepted 12 July 2006
Available online 18 July 2006

**Abstract**

Two doubly charged transition metal complexes, $Pt(CN)_4^{2-}$ and $Pt(CN)_6^{2-}$ commonly found in the condensed phases, are produced as isolated species from solutions to the gas phase using electrospray ionization. Their stability and electronic structures are investigated by photodetachment photoelectron spectroscopy and density functional theory (DFT) calculations. The adiabatic electron detachment energies for the dianions to monoanions are measured to be 1.69 and 3.85 eV for $Pt(CN)_4^{2-}$ and $Pt(CN)_6^{2-}$, respectively. The magnitude of the repulsive Coulomb barrier is estimated to be ~2.5 eV for $Pt(CN)_4^{2-}$, and ~1.7 eV for $Pt(CN)_6^{2-}$. Well-resolved and distinct peaks are observed in the spectra, yielding rich electronic structure information for these complexes. DFT calculations including scalar relativistic and spin–orbit effects are carried out to determine the geometries and to interpret the observed spectral features. The calculations show that the frontier occupied molecular orbitals are largely metal-based for $Pt(CN)_4^{2-}$ and ligand-based for $Pt(CN)_6^{2-}$, in contrast to the standard ligand field theory description.


*Keywords:* Multiply charged anion; Repulsive Coulomb barrier; Cyanide ligand; Platinum coordination complex; Spin–orbit coupling

## 1. Introduction

Multiply charged anions (MCAs) are usually rather fragile as isolated species due to the strong intramolecular Coulomb repulsion among the excess charges. Despite their ubiquity in the condensed phases, isolated MCAs had been difficult to study and very few of them had been known in the gas phase previously [1,2]. Significant advances have been made in the investigation of free MCAs during the past 10 years both theoretically [3–9] and experimentally [10–20]. Very recently, several interesting new experimental findings have been reported, including the observation of the elusive $LiF_3^{2-}$ [21] that was predicted theoretically [9], a series of small dianions produced by sputtering along with gas flooding [22], and the generation of doubly charged anions via charge-transfer [23,24]. Besides the pure mass spectrometry observation, several spectroscopic techniques in conjunction with electrospray ionization have been developed to investigate MCAs, including photoelectron spectroscopy (PES) [10–14,25], photodissociation spectroscopy [26], and photodetachment spectroscopy with variable photon energies [27]. PES is ideal for probing the intrinsic properties of free MCAs and directly yields information about their stability, intramolecular Coulomb repulsion, and solvent stabilization [10].

* Corresponding authors.
*E-mail addresses:* junli@tsinghua.edu.cn (J. Li), ls.wang@pnl.gov (L.-S. Wang).

0301-0104/$ - see front matter © 2006 Elsevier B.V. All rights reserved.
doi:10.1016/j.chemphys.2006.07.018

Most inorganic metal complexes exist in solutions and solid materials as MCAs, which are stabilized by solvents, or counterions. While these species have been studied extensively in the condensed phase, gas phase studies would also be desirable because they provide intrinsic molecular properties without the complications of the condensed phase environments. Gas-phase molecular and spectroscopic information can be used to compare directly with theoretical calculations, which are often done on gaseous species. Using our electrospray PES facility, we have studied in the gas phase two classes of transition metal complexes: the square-planar $MX_4^{2-}$ (M = Pt, Pd; X = Cl, Br) [28,29] and octahedral $MX_6^{2-}$ (M = Re, Os, Ir, Pt; X = Cl, Br) [30], providing detailed electronic structure information on these classical metal complexes. Our work on $MX_6^{2-}$ has stimulated two recent theoretical studies [31,32], which demonstrated the important interplay of electron correlation and relativistic effects.

The tetracynoplatinate, $Pt(CN)_4^{2-}$, and hexacynoplatinate, $Pt(CN)_6^{2-}$ are classical Werner-type transition metal complexes [33], and $Pt(CN)_4^{2-}$ forms interesting one-dimensional ladder structures [34]. There is an extensive body of literature on the properties of these species. Their ground state electronic energy levels have been investigated in numerous studies of optical absorption and magnetic circular dichroism [35–37]. The geometry structures have been determined to be square-planar for $Pt(CN)_4^{2-}$ and octahedral $Pt(CN)_6^{2-}$, as expected from crystal field theory [34,35]. There are several theoretical studies on $Pt(CN)_4^{2-}$, with various approximate molecular orbital approaches and ligand field theory [38,39]. The $Pt(CN)_4^{2-}$ and $Pt(CN)_6^{2-}$ dianions have been observed in the gas phase recently using electrospray and studied using electron scattering and collision induced dissociation [40].

Here we report a combined experimental and theoretical study of $Pt(CN)_4^{2-}$ and $Pt(CN)_6^{2-}$ in the gas phase. They are produced by electrospray and experimentally investigated using PES. The electron binding energies are positive for both dianions and are higher than the corresponding halide complexes reported earlier [28–30], confirming the electronic stability of these species due to the strong electron withdrawing ability of the CN ligands. The experimental data are interpreted with the aid of density functional theory (DFT) calculations including scalar relativistic and spin–orbit coupling effects. The combined experimental and computational data provide direct insight into the electronic structure of these complexes.

## 2. Experimental and theoretical details

### 2.1. Photodetachment photoelectron spectroscopy

The PES experiments were carried out on a home-built instrument that couples an electrospray ionization source (ESI) to a magnetic bottle time-of-flight photoelectron spectrometer [41]. The anions of $Pt(CN)_n^{2-}$ ($n = 4, 6$) were generated by electrospray from 1 mM solutions of $K_2[Pt(CN)_n]$ in a mixed solvent of $H_2O/CH_3OH$ (1/3). Experiments on $Pt(CN)_4^{2-}$ were repeated on a newly built instrument with better resolution due to a longer electron flight tube and more importantly the ability to cool ions to low temperatures [42,43]. The higher resolution was necessary for $Pt(CN)_4^{2-}$ due to the high kinetic energies of the detached electrons as a result of its low electron binding energies. The ESI source and the magnetic-bottle photoelectron spectrometer are similar to that described previously [41]. A key feature of the new instrument is its cooling capability, accomplished by attaching the cold head of a close cycle helium refrigerator to the ion trap, where ions are accumulated and cooled via collisions with a cold background gas. Previous experiments suggest a 70 K nominal trap temperature corresponds to an effective ion temperature of about 70–100 K [42,43]. The cooled ions were pulsed out of the trap into the extraction zone of a time-of-flight mass spectrometer at a 10 Hz repetition rate. Ions of interest were mass selected and decelerated before being intercepted by a detachment laser beam [193 nm (6.424 eV) and 157 nm (7.866 eV) from an excimer laser or 266 nm (4.661 eV) from a Nd:YAG laser] in the interaction zone of the magnetic-bottle photoelectron analyzer. The lasers were operated at a 20 Hz repetition rate with the ion beam off at alternate shots for background subtraction. It took 60,000 to 100,000 total laser shots (cycles) to get a good statistic count rate for each spectrum. Photoelectrons were collected with high efficiency by the magnetic-bottle and analyzed in a 5.2-m long electron flight tube. Photoelectron time-of-flight spectra were collected and then converted into kinetic energy spectra, calibrated by the known spectra of $I^-$ and $ClO_2^-$. Electron binding energy spectra were obtained by subtracting the kinetic energy spectra from the detachment photon energies, followed by a constant energy smoothing procedure (5 meV for 266 nm, 10 meV for 193 and 157 nm). Energy resolution ($\Delta E/E$) was estimated to be approximately 2% (FWHM), i.e. approximately 20 meV for 1 eV electrons, as measured from the spectra of $I^-$ at 355 nm.

### 2.2. Theoretical calculations

The density functional theory (DFT) calculations were carried out using the hybrid B3LYP method, and Becke's three-parameter exchange functional and Lee–Yang–Parr correlation functional [44–46]. The Stuttgart small-core pseudopotential and (8s7p6d)/[6s5p3d] Gaussian basis sets were used for Pt, and 6-31+G(d) all-electron basis sets were used for C and N [47,48]. Scalar relativistic effects (i.e., mass–velocity and Darwin effects) were taken into account via the quasi-relativistic pseudopotentials [47]. The geometries were fully optimized using analytical energy gradients and vibrational frequency calculations were performed to verify that these species are minima on the potential energy surfaces. All these calculations were accomplished using the NWChem 4.7 program [49].

The spin–orbit coupling effects are important for electronic structures of heavy-element complexes [50]. We performed further two-component relativistic DFT calculations using Amsterdam Density Functional code (ADF 2005.01) [51]. The scalar-relativistic effects and spin–orbit coupling effects were included by the zero-order regular approach (ZORA) [52]. The calculations were carried out at the level of generalized gradient approach (GGA) using the exchange–correlation functional of Perdew–Wang 1991 (PW91) [53]. The frozen core approximation was applied to the $[1s^2–4f^{14}]$ core for Pt and $[1s^2]$ cores for C and N. These calculations used the uncontracted Slater basis sets with the quality of triple-zeta plus two polarization functions (TZ2P), i.e., with p- and f-type polarization functions for Pt and d- and f-type polarization functions for C and N [54]. For consistency the geometries were reoptimized with PW91 functional and scalar-relativistic ZORA. The single-point spin–orbit calculations were performed at these optimized geometries. The atomic charges are important in understanding the electron density distributions in these dianionic gas-phase molecules and were calculated via the population analysis formalisms of Mulliken [55], Hirshfeld [56], Voronoi deformation density (VDD) [57], and the multipole derived charge analysis up to quadruple (MDC-q) [58]. All the calculations done with ADF used high integration accuracy (integration = 6.0) and tight convergence criteria of $10^{-5}$ a.u. for energy gradients during geometry optimizations.

## 3. Experimental results

### 3.1. Photoelectron spectra of $Pt(CN)_n^{2-}$ $(n = 4, 6)$

PES spectra of $Pt(CN)_4^{2-}$ were carried out at 266 and 193 nm using both our room- and low-temperature instruments, whereas the $Pt(CN)_6^{2-}$ spectra were taken at 193 and 157 nm using the room-temperature apparatus only. Fig. 1 shows the 70 K spectra of $Pt(CN)_4^{2-}$ at 266 and 193 nm, and Fig. 2 displays the room temperature spectra of $Pt(CN)_6^{2-}$ at 193 and 157 nm. The 70 K spectra of $Pt(CN)_4^{2-}$ are better resolved than the spectra recorded with the room-temperature apparatus (not shown), particularly the first peak at the lowest binding energy is resolved into two components (X and A) in the 70 K data. All resolved peaks are labeled as X, A, B, etc. and their vertical detachment energies are given in Table 1. The adiabatic detachment energies for the X band, i.e. the second electron affinities for $Pt(CN)_4^{2-}$ and $Pt(CN)_6^{2-}$ are given in Table 2 and compared with theoretical calculations.

### 3.2. $Pt(CN)_4^{2-}$

Nine features are resolved in the 193 nm spectrum (X, A–H) for $Pt(CN)_4^{2-}$. At 266 nm, the X and A are better resolved. In the 266 nm spectrum, the strong B and C features almost disappear and the other higher binding energy

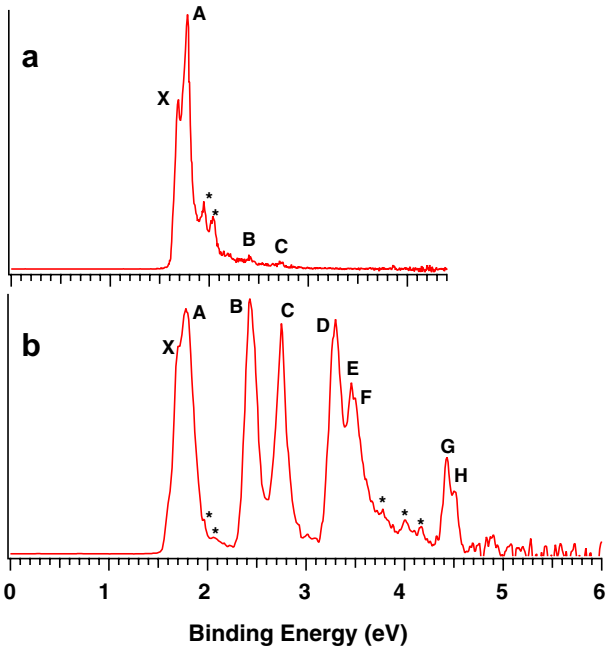


Fig. 1. Photoelectron spectra of $Pt(CN)_4^{2-}$ at 266 nm (a) and 193 nm (b).

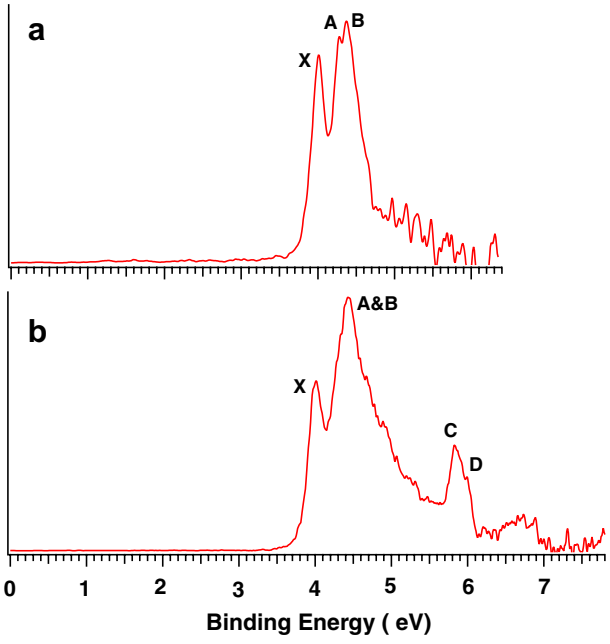


Fig. 2. Photoelectron spectra of $Pt(CN)_6^{2-}$ at 193 nm (a) and 157 nm (b).

Table 1
Vertical detachment energies (VDE in eV) of all the detachment features observed in the PES spectra of $Pt(CN)_n^{2-}$ $(n = 4, 6)$[a]

| | X | A | B | C | D | E | F | G | H |
|---|---|---|---|---|---|---|---|---|---|
| $Pt(CN)_4^{2-}$ | 1.69 | 1.78 | 2.42 | 2.75 | 3.30 | 3.46 | 3.50 | 4.43 | 4.51 |
| $Pt(CN)_6^{2-}$ | 4.01 | 4.28 | 4.37 | 5.8 | 6.0 | | | | |

All labels are referred to Figs. 1 and 2.
[a] The uncertainties for the VDE's are ±0.05 eV.

Table 2
Measured and calculated adiabatic electron binding energies (ADE), the first vertical detachment energies (VDE), and estimated repulsive Coulomb barriers (RCB) for $Pt(CN)_4^{2-}$ and $Pt(CN)_6^{2-}$ [a]

| | $Pt(CN)_4^{2-}$ | $Pt(CN)_6^{2-}$ |
|---|---|---|
| ADE[b,c] | | |
| PW91 | 1.52 | 3.15 |
| B3LYP | 1.91 | 3.76 |
| Experimental | 1.69 (0.05) | 3.85 (0.05) |
| $VDE_1$ | | |
| PW91 | 1.53 | 3.21 |
| B3LYP | 1.95 | 3.81 |
| Experimental | 1.69 | 4.01 |
| RCB | | |
| Experimental | ~2.5 | ~1.7 |

[a] All the energies are in eV. The PW91 results are from ADF calculations and the B3LYP results are from NWChem calculations.
[b] Determined approximately by drawing a straight line at the front edge of the X features and then adding a constant to the intercept with the binding energy axis, to take into account both the instrumental resolution and a finite thermal effect, particularly for the room temperature spectra.
[c] Also represents the adiabatic electron affinity of the singly charged anion. The numbers in the parentheses indicate the uncertainties.

peaks (D–H) are completely missing due to the repulsive Coulomb barrier (RCB) present in MCAs. The two small peaks at 2 eV denoted with '*' are more pronounced at 266 nm, but also existed in the 193 nm spectrum, which displays three more weak features around 4 eV (labeled with '*'). These features may be due to the autodetachment or multiple electron transitions as we observed before in other metal complexes systems [59]. However, without additional high resolution experiments the exact nature of these features is not clear at this point. The electron binding energy of the second electron for $Pt(CN)_4^{2-}$ is 1.69 eV, confirming its electron stability in the gas phase.

### 3.3. $Pt(CN)_6^{2-}$

The spectra of $Pt(CN)_6^{2-}$ are more congested. Five features were observed, i.e.: X at 4 eV, A and B at 4.4 eV, and C and D at 5.8 eV. The A and B peaks shown as one broad feature at 157 nm were partially resolved as two peaks at 193 nm. The spectral cutoff at 193 nm due to the RCB was clearly observed. The lowest vertical detachment energy of $Pt(CN)_6^{2-}$ is 4.01 eV, which is remarkably high for a doubly charged anion. This reflects the high electronic stability of the $Pt(CN)_6^{2-}$ complex.

## 4. Theoretical results

From the familiar crystal field theory, the metal (M) d-orbitals in a $MX_n$ complex are pushed up to become the frontier occupied orbitals, whereas the ligand orbitals are stabilized because of the orbital interactions between the metal and the ligand. In square-planar $MX_4$ complexes the d-orbitals of the central metal are split as $e_g$ $(xz, yz) < a_{1g}$ $(z^2) < b_{2g}$ $(xy) \ll b_{1g}$ $(x^2 - y^2)$, which can accommodate 8 d-electrons to form a stable square-planar complex. Similarly the M d-orbitals split as $t_{2g}$ $(xz, yz, xy) \ll e_g$ $(z^2, x^2 - y^2)$ in $MX_6$-type octahedral complexes, which will form close-shell complexes with $d^6$-configuration. In $Pt(CN)_4^{2-}$ and $Pt(CN)_6^{2-}$, the formal oxidation states of the central metal are Pt(II) and Pt(IV) with a $d^8$ and $d^6$ configurations, and they are expected to be perfect square-planar and octahedral, respectively.

Our calculations show that indeed free $Pt(CN)_4^{2-}$ adopts a square-planar structure with $D_{4h}$ symmetry, whereas $Pt(CN)_6^{2-}$ has a perfect octahedral ($O_h$) structure, the same as found in the condensed phases. These structures are confirmed to be minima from vibrational frequency calculations. Geometry optimization of these species with lower symmetry all converged to the $D_{4h}$ and $O_h$ symmetries, respectively, indicating that these are the global minima structures for the dianions. Table 3 shows the calculated MO contour surfaces and Pt orbital percentages of these two close-shell molecules; only the frontier occupied MOs and those containing Pt d-orbital characters are included. The molecular symmetries, electronic states, and optimized bond lengths of $Pt(CN)_n^{2-}$ and $Pt(CN)_n^{-}$ $(n = 4, 6)$ are listed in Table 4. We also calculated the atomic net charges based on Mulliken, Hirshfeld, Voronoi, and MDC-q formalisms, as listed in Table 5.

The determination of the correct ground-state geometries of $Pt(CN)_n^{-}$ $(n = 4, 6)$ monoanions are quite complicated because of the strong spin-polarization, Jahn–Teller effects, and spin-orbit coupling effects in these open-shell heavy-element systems. While the exact treatment of these open-shell species would require multi-configuration methods, our DFT calculations have provided results that are reasonably close to the experimental data. We have performed comprehensive searches of the possible Jahn–Teller distorted structures of the $Pt(CN)_n^{-}$ $(n = 4, 6)$ monoanions by following the vibrational imaginary modes and the subgroups of the molecular point-groups of the dianions. The $Pt(CN)_4^{-}$ ion has a $^2E_g$ ground state, which is formed when an electron is detached from the HOMO − 1 $2e_g$ orbital of the dianion. The electronic states formed by removing electron from other frontier MOs have higher energies, which have been confirmed by further TDDFT calculations. When spin–orbit effects are included, the degeneracy of this $^2E_g$ state is removed so that the monoanion retains the $D_{4h}$ symmetry as its dianion parent.

The molecular orbital energy levels of the two dianions (Fig. 3) were calculated using PW91 functional considering both scalar relativistic effects and spin–orbit splitting. As shown in Table 3, the HOMO of $Pt(CN)_4^{2-}$ is an $a_{1g}$ orbital predominantly from Pt 5d (75%) and 6s (21%) orbitals, HOMO − 1 is a doubly degenerate $e_g$ orbital consisting of 59% Pt 5d orbitals, and HOMO − 2 is a $b_{2g}$ orbital with 44% Pt 5d orbitals. The occupation of these MOs provides the foundation of the familiar $d^8$ electron configuration for $Pt(CN)_4^{2-}$. HOMO − 3 to HOMO − 9 are mainly ligand-based orbitals, which are followed by the four low-energy

Table 3
MO symmetries, contour surfaces, and percentages of Pt orbitals of some occupied frontier MOs of the $D_{4h}$ $Pt(CN)_4^{2-}$ and $O_h$ $Pt(CN)_6^{2-}$ dianions[a]

| | $Pt(CN)_4^{2-}$ | | | $Pt(CN)_6^{2-}$ | | |
|---|---|---|---|---|---|---|
| | Symmetry | MO | Pt% | Symmetry | MO | Pt% |
| HOMO | $5a_{1g}$ |  | 75%d 21%s | $2t_{2g}$ | 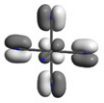 | 27%d |
| HOMO – 1 | $2e_g$ | 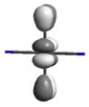 | 59%d | $5t_{1u}$ | 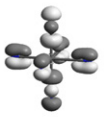 | 3%p |
| HOMO – 2 | $2b_{2g}$ |  | 44%d | $1t_{1g}$ | 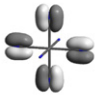 | 0% |
| HOMO – 3 | $5e_u$ | 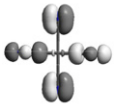 | 5%p | $1t_{2u}$ | 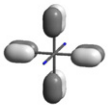 | 0% |
| HOMO – 4 | $1a_{2g}$ |  | 0% | $4t_{1u}$ |  | 4%p |
| Pt d | $1e_g$ |  | 34%d | $1t_{2g}$ | 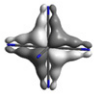 | 68%d |
| Pt d | $1b_{2g}$ |  | 47%d | $2e_g$ | 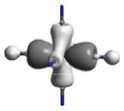 | 52%d |
| Pt d | $2b_{1g}$ | 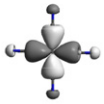 | 45%d | | | |
| Pt d | $3a_{1g}$ |  | 23%d | | | |

[a] The ligand orbitals lying between the MOs with Pt d-characters are not shown. The percentages of the MOs are from PW91 (ADF) calculations.

Table 4
Molecular symmetries, ground states, and optimized bond distances of $M(CN)_n^q$ ($n = 4, 6$; $q = -2, -1$) as calculated using PW91 (ADF)

| | Symmetry | State | Pt–C | C–N |
|---|---|---|---|---|
| $Pt(CN)_4^{2-}$ | $D_{4h}$ | $^1A_{1g}$ | $2.01 \times 4$ | $1.17 \times 4$ |
| $Pt(CN)_4^{-}$ | $D_{4h}$ | $^2E_g$ | $1.99 \times 4$ | $1.17 \times 4$ |
| $Pt(CN)_6^{2-}$ | $O_h$ | $^1A_{1g}$ | $2.04 \times 6$ | $1.17 \times 6$ |
| $Pt(CN)_6^{-}$ | $C_s$ | $^2A'$ | $2.02 \times 4$ | $1.17 \times 4$ |
| | | | 2.01, 2.04 | 1.17, 1.16 |

orbitals (1 $e_g$, $1b_{2g}$, $2b_{1g}$, and $3a_{1g}$), shown in Table 3, that have significant amount of Pt d-orbital characters, indicating strong covalent metal–ligand orbital interactions. This is consistent with the textbook ligand-field description for this type of complexes, i.e., the metal d orbitals are energetically pushed up as the occupied frontier MOs due to the electrostatic repulsion from the surrounding ligands. Since the highest occupied MOs are mainly metal-based orbitals, the spin–orbit splittings are large so that the Jahn–Teller distortion of the $Pt(CN)_4^-$ ion is quenched and the mono-anion retains the $D_{4h}$ symmetry.

On the contrary, while ligand-field description predicts the highest occupied $t_{2g}$ orbitals of $Pt(CN)_6^{2-}$ should be mainly composed of Pt 5d orbitals, corresponding to the $d^6$ configuration, DFT calculations indicate that the HOMO $t_{2g}$ only have 27% d-orbital character. There are much higher Pt 5d-orbital characters in two low-energy orbitals, $1t_{2g}$ (68%) and $2e_g$ (52%). In other words, the HOMO is mainly ligand-based and thus the spin-orbit splitting is expected to be much smaller in $Pt(CN)_6^{2-}$ than in the $Pt(CN)_4^{2-}$ complex. Indeed our calculations reveal that spin–orbit splitting of the $2e_g$ MO in $Pt(CN)_4^{2-}$ is

Table 5
Calculated net charges based on Mulliken, Hirshfeld, Voronoi, and MDC-q formalisms[a]

| | $D_{4h}$ $Pt(CN)_4^{2-}$ | | | $O_h$ $Pt(CN)_6^{2-}$ | | |
|---|---|---|---|---|---|---|
| | Pt | C | N | Pt | C | N |
| Mulliken | −0.18 | −0.02 | −0.44 | 0.28 | −0.01 | −0.37 |
| Hirshfeld | 0.19 | −0.14 | −0.41 | 0.45 | −0.07 | −0.33 |
| Voronoi | 0.24 | −0.14 | −0.42 | 0.53 | −0.09 | −0.34 |
| MDC-q | 0.30 | −0.02 | −0.55 | 0.90 | −0.04 | −0.44 |
| | $D_{4h}$ $Pt(CN)_4^-$ | | | $C_s$ $Pt(CN)_6^-$ | | |
| Mulliken | 0.46 | −0.08 | −0.29 | 0.32 | $0.04 \sim 0.05$ | $-0.25 \sim -0.27$ |
| Hirshfeld | 0.35 | −0.08 | −0.26 | 0.50 | $-0.02 \sim -0.04$ | $-0.20 \sim -0.23$ |
| Voronoi | 0.42 | −0.10 | −0.25 | 0.57 | $-0.05 \sim -0.07$ | $-0.25 \sim -0.28$ |
| MDC-q | 0.73 | −0.12 | −0.31 | 1.07 | $-0.77 \sim -0.88$ | $0.24 \sim 0.46$ |

[a] All these charges are calculated from PW91 (ADF). The MDC-q charges are oscillating for $C_s$ $Pt(CN)_6^-$, with the charges on C and N of the elongated CN group in the reversed signs to those of the other CN groups.

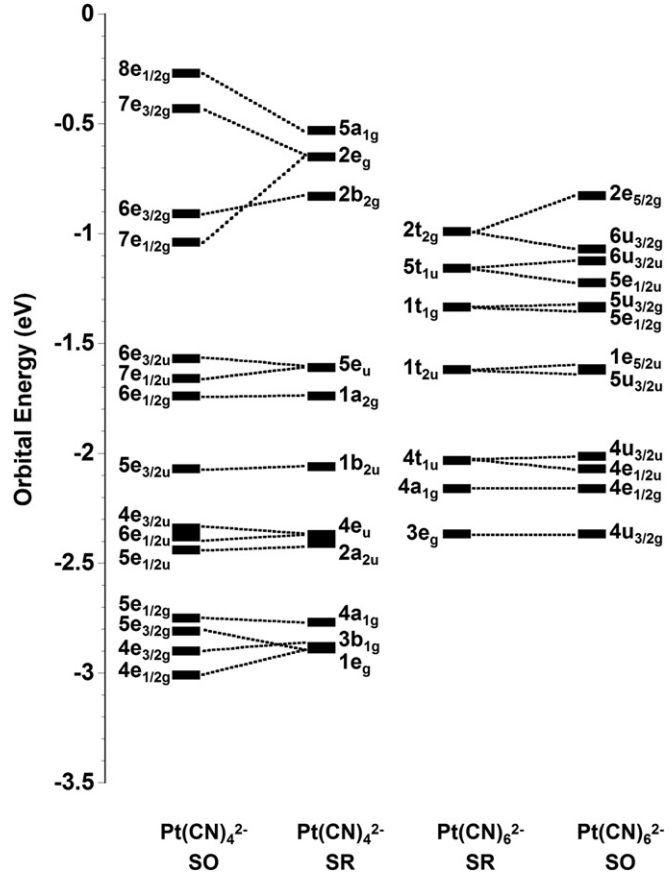


Fig. 3. Scalar-relativistic and spin–orbit coupled energy levels of $Pt(CN)_4^{2-}$ and $Pt(CN)_6^{2-}$ calculated using PW91 and ZORA (see computational methods for details). The levels of $Pt(CN)_4^{2-}$ are shifted down by 1.691 eV to align with those of $Pt(CN)_6^{2-}$.

0.61 eV, whereas that of the $2t_{2g}$ MO is only 0.24 eV, as shown in Fig. 3. It is therefore likely that the Jahn–Teller effects will prevail over the spin–orbit splitting, leading to a low-symmetry structure for the $Pt(CN)_6^-$ species, which is formed when an electron is detached from the ligand-based HOMO.

To determine the lowest-energy structure of $Pt(CN)_6^-$ we searched a series of geometries with symmetries of $D_{4h}$, $D_{3d}$, and their subgroups. The ground-state geometry is found to have only $C_s$ symmetry. Although the overall structure is close to octahedron, all the diagonal ∠CPtC bond angles are around 174–175° even at very tight convergence criteria for geometry optimization. The most significant geometry change occurs for the Pt–C bond distances. All the four Pt–C bond lengths in the equatorial plane are around 2.02 Å, while one of the axial Pt–C bond is shortened (2.01 Å) and the other axial Pt–C bond is elongated (2.04 Å), showing small but non-negligible *trans influence*. As a result, the four equatorial Pt–C bonds are slightly bent toward the elongated Pt–C bond. This geometry change from $O_h$ to $C_s$ upon electron detachment is consistent with the broad band in the PES spectra of the $Pt(CN)_6^{2-}$ complex.

Using these structures obtained for the dianions and monoanions, we calculated the adiabatic detachment energies (ADE) and the first vertical detachment energies ($VDE_1$) of the $Pt(CN)_n^{2-}$ ($n = 4, 6$) complexes. The calculated results from PW91 (ADF) and B3LYP (NWChem) are given in Table 2. The calculated ADE and $VDE_1$ are in reasonable agreement with the experiments, but quantitative agreement cannot be reached at these levels of the DFT theory because the self-interaction error (SIE), inherent to the approximate exchange–correlation functionals used, is large for these small-size but highly negatively charged species. The hybrid DFT method (B3LYP) performs slightly better than the pure GGA method (PW91), as is expected for systems with large SIE.

## 5. Discussion

### 5.1. Spectral assignments

Accurate calculations and assignments of PES spectra are a great challenge in computational chemistry because in principle one needs to accurately calculate the total energies of the electronic ground state of the parent species and the electronic ground state and excited states of the electron-detached species. At present such calculations including multi-configurations and spin–orbit coupling are

difficult. However, within a one-electron formalism, the observed PES features can be approximately viewed as removing electrons from the occupied MOs of $Pt(CN)_n^{2-}$. The ground states of the two dianions are calculated to be closed-shell with $^1A_{1g}$ symmetry, and the final states of the singly charged anion are all doublet states. When electronic relaxation upon electron detachment is ignored, the features revealed in the PES spectra provide a direct mapping of the occupied MO energy levels of the $Pt(CN)_n^{2-}$ parent dianions. We will therefore use the calculated Kohn–Sham (KS) MO energy levels of the dianions to qualitatively interpret the observed PES spectra. Although KS orbitals are different from the Hartree–Fock orbitals and Koopman's theorem is not valid for DFT orbital energies, DFT orbitals and orbital energies are useful in qualitatively understanding the MO ordering and the PES spectra because they also include electron correlation effects within a one-electron formalism [60–62].

Based on the above discussion and Fig. 3, the first four features (X, A, B, and C) observed in the PES spectra of $Pt(CN)_4^{2-}$ are assigned to electron detachment from the $8e_{1/2g}$, $7e_{3/2g}$, $6e_{3/2g}$, and $7e_{1/2g}$ spin orbitals, respectively. The energy level spacing pattern of these four orbitals is in accord with the observed peak pattern, i.e., the X and A are nearly degenerate, then there is an energy gap followed by the B and C peaks. The observed energy gap between C and D are also well illustrated by the energy level diagram, which shows a gap between $7e_{1/2g}$ and $6e_{3/2u}$. The other observed peaks D, E, F correspond to removing electrons from the deep spin orbitals $6e_{3/2u}$, $7e_{1/2u}$, $6e_{1/2g}$. The two weak features at ~2 eV observed in the 266 and 193 nm spectra (labeled *), and three more at ~4 eV in the 193 nm spectrum are likely due to autodetachment transitions. These are presumed to arise through absorption of a photon by $Pt(CN)_4^{2-}$ to a metastable electronically excited states of the parent dianion that lies above the detachment threshold, which can undergo significant vibrational relaxation prior to electron detachment. Similar autodetachment was observed in other metal complexes [59].

The assignment of the PES spectra of $Pt(CN)_6^{2-}$ is more difficult because of the geometry changes caused by the Jahn–Teller effects in the final states and the spectral congestion, which is consistent with the closely spaced MOs (Fig. 3). The X peak is due to detaching one electron from the spin orbital $2e_{5/2g}$, which is well separated from the others because of spin–orbit coupling. The broad feature of A and B is likely due to the overlapping of many transitions, namely by removing electrons from $6u_{3/2g}$, $6u_{3/2u}$, $5e_{1/2u}$, $5u_{3/2g}$, $5e_{1/2g}$, $1e_{5/2u}$, and $5u_{3/2u}$, which are close in energy. It is interesting to note that the decreasing intensity of the broad A and B band is consistent with the calculated orbital characters: among these frontier spin orbitals $2e_{5/2g}$ and $6u_{3/2g}$ have contribution from Pt d-orbitals, while others are purely ligand-based orbitals. The C and D are probably from removing electrons from the next group of MOs that are well separated from $5u_{3/2u}$ by a large energy gap, i.e. $4u_{3/2u}$, $4e_{1/2u}$, and $4e_{1/2g}$. While the spin–orbit coupled energy levels well represent the energy gaps observed in the experimental PES spectra, state-specific calculations including spin–orbit coupling effects are needed to interpret the spectra on a more quantitative basis.

### 5.2. The repulsive Coulomb barrier (RCB) and intramolecular Coulomb repulsion

There is an essential difference between photodetachment of MCAs and singly charged anions. When an electron is removed from an MCA, the two photoproducts, a free electron and an anion with one less charge than the parent MCA, are both negatively charged. The superposition of the long range Coulomb repulsion between the outgoing electron and the remaining anion and the short-range electron binding produces an effective potential barrier for the outgoing electron. The RCB has a profound effect on MCAs, providing a dynamical stability for the MCAs, even when they are thermodynamically unstable [10–14].

In principle, the RCB is very complicated because it is anisotropic, non-local, and dependent on the electron kinetic energy [63]. Several theoretical models have been developed trying to calculate the RCB [63,64]. In general, each detachment channel has its own RCB, which may have different magnitudes as being demonstrated for the benzene dicarboxylate dianions where the detached electrons are from different parts of the molecules and thus experience slightly different Coulomb repulsion [65]. Since $Pt(CN)_n^{2-}$ are relatively small dianions, if we assume that the RCB is the same for different detachment channels, we can estimate the magnitude of their RCB based on the photon energy dependence of appearance or disappearance of PES features on the high binding energy side.

Fig. 1 shows that the intense B-peak at 193 nm almost completely disappears at 266 nm, suggesting that the 266-nm photon energy is below the RCB of the B-band, i.e. RCB > 2.2 eV (photon energy – B-band binding energy, i.e., 4.66–2.42 eV). On the other hand, the A-peak does not seem to be affected at 266 nm, indicating that the 266 nm photon energy is above the RCB of the A channel, i.e. RCB < 2.88 eV (4.66–1.78). Therefore we can bracket the RCB of $Pt(CN)_4^{2-}$ as 2.2 eV < RCB < 2.8 eV, or ~2.5 eV, which can be compared with the empirically calculated values between 1.5 and 3 eV [40].

The spectra of $Pt(CN)_6^{2-}$ has less distinct peaks to allow us to perform the same bracketing of RCB. Careful comparison of the 193 nm spectrum with that at 157 nm indicates a spectral cutoff at 4.7 eV in the 193 nm spectrum. This cutoff gives the RCB of ~1.7 eV (6.42–4.7). The estimated RCBs of $Pt(CN)_4^{2-}$ and $Pt(CN)_6^{2-}$ are comparable to that of $PtX_4^{2-}$ (i.e. 2.5 eV for X = Cl and 2.1 eV for X = Br, measured by PES [28], and 2.0 eV for X = Br by scanning the laser photon energy cross the RCB barrier top [27]) and $PtCl_6^{2-}$ (2.0 eV by PES) [30], respectively.

The smaller RCB height for $Pt(CN)_6^{2-}$ is consistent with the facts that there is less Coulomb repulsion and hence higher electron binding energy for the $Pt(CN)_6^{2-}$ species,

and there are two more ligands to share the extra charges. The first electron detachment energy of $Pt(CN)_6^{2-}$ is much higher than that of $Pt(CN)_4^{2-}$, which is consistent with the Pt–CN bond distance and charge distribution. More detailed analysis shows that the effect due to change of the Pt–CN distance is small, whereas charge distribution plays a major role. As shown in Tables 4 and 5, the negative charges are mainly distributed on the N atoms and the N···N distance is longer in $Pt(CN)_6^{2-}$ than in $Pt(CN)_4^{2-}$, which helps to reduce the Coulomb repulsion in the former.

## 6. Stability of the platinum-cyanide dianionic complexes

It is interesting to compare the electronic stability of $Pt(CN)_n^{2-}$ with the corresponding halide complexes, $PtX_n^{2-}$ (X = Cl, Br). The $PtX_4^{2-}$ complexes possess slightly negative adiabatic electron detachment energies (ADEs), −0.25 eV and −0.04 eV for X = Cl and Br, respectively, and are electronically unstable species [28,29]. The ADE of $Pt(CN)_4^{2-}$ is well above zero (1.69 eV), a highly electronically stable dianion. The ADE of $Pt(CN)_6^{2-}$ was measured to be 3.85 eV, also much higher than that of $PtCl_6^{2-}$ (1.58 eV) and $PtBr_6^{2-}$ (1.52 eV) [30]. In fact, it has the highest ADE among all the dianions we have measured so far (the next one is $ZrF_6^{2-}$ with an ADE of 3.4 eV [66]). It is remarkable to observe such a high ADE from a dianionic species despite the strong intramolecular Coulomb repulsion. The high electronic stability of these cyanide complexes is mainly due to the electron withdrawing capability of the CN ligand.

The high stability of the hexa-coordinate metal complexes relative to the tetra-coordinate one is largely electronic in origin. In $Pt(CN)_6^{2-}$, not only are the extra electrons shared among the six ligands instead of four, but also the Pt atom has a higher positive charge, both of which enhance the electron binding ability. Consistent with the calculated net charges on the CN groups (Table 5), the formal fractional charge that each ligand shared is decreased from 1/2 ($n = 4$) to 1/3 ($n = 6$), thus reducing the Coulomb repulsion among the ligands (~1.7 eV for $n = 6$ vs. ~2.5 eV for $n = 4$).

## 7. Conclusions

We report a combined photoelectron spectroscopic and theoretical study of two inorganic complex dianions, $Pt(CN)_n^{2-}$ ($n = 4, 6$) in the gas phase. The two species are found to be highly electronically stable as isolated species with adiabatic detachment energies of 1.69 eV and 3.85 eV, respectively. Theoretical calculations confirmed that $Pt(CN)_4^{2-}$ adopts a square-planar structure and $Pt(CN)_6^{2-}$ is octahedral in the gas phase same as in the condensed phase. Well-resolved and distinct features are obtained in the PES spectra, and are qualitatively assigned on the basis of the calculated Kohn–Sham molecular orbital energy level, including scalar relativistic effects and spin–orbit coupling.

## Acknowledgements

The experimental work was supported by the US National Science Foundation (CHE-0349426) and performed at the W.R. Wiley Environmental Molecular Sciences Laboratory, a national scientific user facility sponsored by DOE's Office of Biological and Environmental Research and located at Pacific Northwest National Laboratory, which is operated for DOE by Battelle. The theoretical work was supported by the National Natural Science Foundation of China (20525104) and the calculations were performed by using a HP Itanium2 Linux cluster at the National Laboratory for Information Science and Technology at Tsinghua University.

## References

[1] W.P.M. Maas, N.M.M. Nibbering, Int. J. Mass Spectrom., Ion Processes 88 (1989) 257.
[2] G.R. Freeman, N.H. March, J. Phys. Chem. 100 (1996) 4331.
[3] M.K. Scheller, R.N. Compton, L.S. Cederbaum, Science 270 (1995) 1160.
[4] A.I. Boldyrev, M. Gutowski, J. Simons, Acc. Chem. Res. 29 (1996) 497.
[5] V.G. Zakrzewski, J.V. Ortiz, J. Chem. Phys. 102 (1995) 294.
[6] A. Dreuw, L.S. Cederbaum, Chem. Rev. 102 (2002) 181.
[7] C. Yannouleas, U. Landman, Chem. Phys. Lett. 210 (1993) 437.
[8] J.D. Watts, R.J. Bartlett, J. Chem. Phys. 97 (1992) 3445.
[9] M.K. Scheller, L.S. Cederbaum, Chem. Phys. Lett. 216 (1993) 141.
[10] L.S. Wang, X.B. Wang, J. Phys. Chem. A 104 (2000) 1978; X.B. Wang, X. Yang, L.S. Wang, Int. Rev. Phys. Chem. 21 (2002) 473.
[11] X.B. Wang, C.F. Ding, L.S. Wang, Phys. Rev. Lett. 81 (1998) 3351.
[12] C.F. Ding, X.B. Wang, L.S. Wang, J. Phys. Chem. A 102 (1998) 8633.
[13] X.B. Wang, L.S. Wang, Nature 400 (1999) 245.
[14] X.B. Wang, X. Yang, J.B. Nicholas, L.S. Wang, Science 294 (2001) 1322.
[15] C. Jin, R.L. Hettich, R.N. Compton, A.A. Tuinman, A. Derecskei-Kovacs, D.S. Marynick, B.I. Dunlap, Phys. Rev. Lett. 73 (1994) 2821.
[16] R.N. Compton, A.A. Tuinman, C.E. Klots, M.R. Pederson, D.C. Patton, Phys. Rev. Lett. 78 (1997) 4367.
[17] C. Yannouleas, U. Landman, A. Herlert, L. Schweikhard, Phys. Rev. Lett. 86 (2001) 2996.
[18] S.N. Schauer, P. Williams, R.N. Compton, Phys. Rev. Lett. 65 (1990) 625.
[19] J. Klein, R. Middleton, Nucl. Instr. Meth. Phys. Res. B 159 (1999) 8.
[20] R. Middleton, J. Klein, Phys. Rev. A 60 (1999) 3515.
[21] X.L. Zhao, A.E. Litherland, Phys. Rev. A 71 (2005) 064501.
[22] K. Franzreb, P. Williams, J. Chem. Phys. 123 (2005) 224312.
[23] B. Liu, S. Tomita, J. Rangama, P. Hvelplund, S.B. Nielsen, ChemPhysChem 4 (2003) 1341.
[24] B. Liu, P. Hvelplund, S.B. Nielsen, S. Tomita, Phys. Rev. Lett. 92 (2004) 168301.
[25] O.T. Ehrler, F. Furche, J.M. Weber, M.M. Kappes, J. Chem. Phys. 122 (2005) 094321.
[26] J. Friedrich, S. Gilb, O.T. Ehrler, A. Behrendt, M.M. Kappes, J. Chem. Phys. 117 (2002) 2635.
[27] D. Loffler, J.M. Weber, M.M. Kappes, J. Chem. Phys. 123 (2005) 224308.
[28] X.B. Wang, L.S. Wang, J. Am. Chem. Soc. 122 (2000) 2339.

[29] X.B. Wang, L.S. Wang, Phys. Rev. Lett. 83 (1999) 3402.
[30] X.B. Wang, L.S. Wang, J. Chem. Phys. 111 (1999) 4497.
[31] T. Sommerfeld, S. Feuerbacher, M. Pernpointner, L.S. Cederbaum, J. Chem. Phys. 118 (2003) 1747.
[32] M. Pernpointner, J. Breidbach, L.S. Cederbaum, J. Chem. Phys. 122 (2005) 064311.
[33] F.A. Cotton, G. Wilkinson, Advanced Inorganic Chemistry, Wiley, New York, 1988.
[34] D.W. Knoeppel, S.G. Shore, Inorg. Chem. 35 (1996) 5328.
[35] W.R. Mason III, H.B. Gray, J. Am. Chem. Soc. 90 (1968) 5721.
[36] A. Lechner, G. Gliemann, J. Am. Chem. Soc. 111 (1989) 7469.
[37] P.J. Stephens, A.J. McCaffery, P.N. Schatz, Inorg. Chem. 7 (1968) 1923.
[38] H.B. Gray, C.J. Ballhausen, J. Am. Chem. Soc. 85 (1963) 260.
[39] J.R. Perumareddi, A.D. Liehr, A.W. Adamson, J. Am. Chem. Soc. 85 (1963) 249.
[40] M.O. El Ghazaly, A. Svendsen, H. Bluhme, A.B. Nielsen, S. Brøndsted Nielsen, L.H. Andersen, Phys. Rev. Lett. 93 (2004) 203201; G. Bojesen, P. Hvelplund, T.J.D. Jorgensen, S.B. Nielsen, J. Chem. Phys. 113 (2000) 6608.
[41] L.S. Wang, C.F. Ding, X.B. Wang, S.E. Barlow, Rev. Sci. Instrum. 70 (1999) 1957.
[42] X.B. Wang, H.K. Woo, B. Kiran, L.S. Wang, Angew. Chem., Int. Ed. 44 (2005) 4968.
[43] X.B. Wang, H.K. Woo, B. Kiran, L.S. Wang, J. Chem. Phys. 123 (2005) 051106.
[44] A.D. Becke, J. Chem. Phys. 98 (1993) 1372;
A.D. Becke, J. Chem. Phys. 98 (1993) 5648.
[45] C. Lee, G. Yang, R.G. Parr, Phys. Rev. B 37 (1988) 785.
[46] (a) P.J. Stephens, F.J. Devlin, C.F. Chabalowski, M.J. Frisch, J. Phys. Chem. 98 (1994) 11623;
(b) P.J. Stephens, F.J. Devlin, C.S. Ashvar, C.F. Chabalowski, M.J. Frisch, Faraday Discuss. 99 (1994) 103.
[47] D. Andrae, U. Häusserman, M. Dolg, H. Stoll, H. Preuss, Theor. Chim. Acta 77 (1990) 123.
[48] R. Ditchfield, W.J. Hehre, J.A. Pople, J. Chem. Phys. 54 (1971) 724.
[49] E. Apra, T.L. Windus, T.P. Straatsma, E.J. Bylaska, W. de Jong, S. Hirata, M. Valiev, M.T. Hackler, L. Pollack, K. Kowalski, R.J. Harrison, M. Dupuis, D.M.A. Smith, J. Nieplocha, V. Tipparaju, M. Krishnan, A.A. Auer, E. Brown, G. Cisneros, G.I. Fann, H. Fruchtl, J. Garza, K. Hirao, R. Kendall, J.A. Nichols, K. Tsemekhman, K. Wolinski, J. Anchell, D. Bernholdt, P. Borowski, T. Clark, D. Clerc, H. Dachsel, M. Deegan, K. Dyall, D. Elwood, E. Glendening, M. Gutowski, A. Hess, J. Jaffe, B. Johnson, J. Ju, R. Kobayashi, R. Kutteh, Z. Lin, R. Littlefield, X. Long, B. Meng, T. Nakajima, S. Niu, M. Rosing, G. Sandrone, M. Stave, H. Taylor, G. Thomas, J. van Lenthe, A. Wong, Z. Zhang, NWChem, A Computational Chemistry Package for Parallel Computers, Version 4.7, Pacific Northwest National Laboratory, Richland, Washington, USA, 2005.
[50] P. Pyykkö, Chem. Rev. 88 (1988) 563.
[51] (a) ADF 2005.01, SCM, Theoretical Chemistry, Vrije Universiteit, Amsterdam, The Netherlands (http://www.scm.com) G. te Velde, F.M. Bickelhaupt, S.J.A. van Gisbergen, C. Fonseca Guerra, E.J. Baerends, J.G. Snijders, T. Ziegler, J. Comput. Chem. 22 (2001) 931;
(b) C. Fonseca Guerra, J.G. Snijders, G. te Velde, E.J. Baerends, Theor. Chem. Acc. 99 (1998) 391.
[52] E. van Lenthe, E.J. Baerends, J.G. Snijders, J. Chem. Phys. 99 (1993) 4597.
[53] (a) J.P. Perdew, Y. Wang, Phys. Rev. B 45 (1992) 13244;
(b) J.P. Perdew, J.A. Chevary, S.H. Vosko, K.A. Jackson, M.R. Pederson, D.J. Singh, C. Foilhais, Phys. Rev. B 46 (1992) 6671.
[54] E. van Lenthe, E.J. Baerends, J. Comp. Chem. 24 (2003) 1142.
[55] (a) R.S. Mulliken, J. Chem. Phys. 23 (1955) 1833;
(b) R.S. Mulliken, J. Chem. Phys. 36 (1962) 3428.
[56] F.L. Hirshfeld, Theor. Chim. Acta 44 (1977) 129.
[57] C. Fonseca Guerra, J.-W. Handgraaf, E.J. Baerends, F.M. Bickelhaupt, J. Comp. Chem. 25 (2004) 189.
[58] M. Swart, P. Th. van Duijnen, J.G. Snijders, J. Comput. Chem. 22 (2001) 79.
[59] T. Waters, H.K. Woo, X.B. Wang, L.S. Wang, J. Am. Chem. Soc. 128 (2006) 4282.
[60] E.J. Baerends, O.V. Gritsenko, J. Phys. Chem. A 101 (1997) 5383.
[61] P. Politzer, F. Abu-Awwad, Theor. Chem. Acc. 99 (1998) 83.
[62] R. Stowasser, R. Hoffmann, J. Am. Chem. Soc. 121 (1999) 3414.
[63] A. Dreuw, L.S. Cederbaum, Phys. Rev. A 63 (2000) 012501.
[64] Q. Shi, S. Kais, J. Am. Chem. Soc. 124 (2002) 11723.
[65] X.B. Wang, J.B. Nicholas, L.S. Wang, J. Chem. Phys. 113 (2000) 653.
[66] X.B. Wang, L.S. Wang, J. Phys. Chem. A 104 (2000) 4429.